Journal of Magnetic Resonance **137,** 324–332 (1999)
Article ID jmre.1998.1674, available online at http://www.idealibrary.com on IDEAL®

Magnetic Resonance Imaging of Gases: A Single-Point Ramped Imaging with T_1 Enhancement (SPRITE) Study

Pablo J. Prado, Bruce J. Balcom,[1] Igor V. Mastikhin, Albert R. Cross, Robin L. Armstrong, and Alan Logan*

*MRI Centre, Department of Physics, P.O. Box 4400, University of New Brunswick, Fredericton, New Brunswick, Canada E3B 5A3; and *Centre for Coastal Studies and Aquaculture, P.O. Box 5050, University of New Brunswick, Saint John, New Brunswick, Canada E2L 4L5*

Received June 19, 1998; revised November 19, 1998

A pure phase-encoding MRI technique, single-point ramped imaging with T_1 enhancement, SPRITE, is introduced for the purpose of gas phase imaging. The technique utilizes broadband RF pulses and stepped phase encode gradients to produce images, substantially free of artifacts, which are sensitive to the gas T_1 and T_2^* relaxation times. Images may be acquired from gas phase species with transverse relaxation times substantially less than 1 ms. Methane gas images, ^{1}H, were acquired in a phantom study. Sulfur hexafluoride, ^{19}F, images were acquired from a gas-filled porous coral sample. High porosity regions of the coral are observed in both the MRI image and an X-ray image. Sensitivity and resolution effects due to signal modulation during the time-efficient acquisition are discussed. A method to increase the image sensitivity is discussed, and the predicted improvement is shown through 1D images of the methane gas phantom.

Key Words: **SPI; SPRITE; gas imaging.**

INTRODUCTION

While intuitively appealing, gas phase MRI has not been actively pursued until quite recently due to a variety of technical challenges which have hindered development of appropriate imaging methods. The most obvious problem is the low spin concentration, reflected in poor image signal-to-noise ratios. In addition, rapid molecular diffusion of gases (the diffusion coefficient is typically five orders of magnitude larger than in the liquid phase) through magnetic field gradients may yield significant signal attenuation. Perhaps more importantly, polyatomic gases containing spin-$\frac{1}{2}$ nuclei have relaxation times which are dominated by the spin-rotation interaction (*1, 2*) which is associated with the electronic structure, magnetic moment, of the molecule. Short relaxation times, typically of the order of milliseconds, are frequently observed as a result of the interaction between the nuclear spin and fluctuating intramolecular magnetic fields produced by rapid molecular rotation (modulated by collisions). The inherently short T_2 relaxation time, combined with additional signal loss due to molecular diffusion through imaging field gradients, severely restricts the use of spin and gradient echo based imaging methods. Nevertheless, fast T_1 relaxation is an opportunity which allows for short repetition times and extensive signal averaging.

In the past few years, gas phase imaging has been explored with two very different experimental methods. Projection reconstruction techniques, introduced by Lauterbur (*3*), have been explored by Kuethe *et al.* (*4*) to image inherently high sensitivity nuclei (fluorine) in the gas phase. Kuethe *et al.* rely on rapid signal averaging to achieve acceptable signal-to-noise. The rapid transverse relaxation of the gas phase species requires RF excitation in the presence of the frequency encoding magnetic field gradient. Not only does this introduce a linewidth restriction on resolution, the spectrometer deadtime prevents detection of the *k*-space origin data. Contrast in projection reconstruction MRI gas phase images will be dependent on local gas densities and the T_1 relaxation time.

The alternative, and more popular, gas phase imaging modality employs largely conventional MRI imaging techniques with spin-hyperpolarized noble gases (*5–9*). The laser hyperpolarization process creates a nonequilibrium magnetization which may be greater than the equilibrium thermal magnetization by a factor of 10^4. These imaging methods, which have primarily found application imaging lung structure and function, are restricted to ^{3}He and ^{129}Xe noble gases. The spherically symmetric electron density surrounding these nuclei precludes spin rotation relaxation and yields T_1 relaxation times, in the pure gas phase, of many hours. Long T_1 relaxation times are required for successful hyperpolarized gas imaging because regression to thermal equilibrium is governed by the T_1 time constant. In realistic porous media, or untreated storage vessels, with significant surface relaxation effects, thermal magnetization will rapidly be reestablished and the hyperpolarization advantage lost.

In this work we present a new way to image gases. A preliminary account of some aspects of this work was recently reported (*10*). The technique, called SPRITE, single-point ramped imaging with T_1 enhancement (*11*), is based on the single-point imaging (SPI) technique (*12*). Pure phase encoding with SPI (*13*) eliminates many of the difficulties encoun-

[1] To whom correspondence should be addressed.

1090-7807/99 $30.00

tered with short T_2^* systems (*11*). A series of recent reports indicates the scope of the technique. Applications to material sciences are reported through studies on cement and concrete (*14, 15*), polymers (*16, 17*), compact bone (*18*), and water adsorption in zeolites (*19*). This near-silent technique is able to generate images which may have quantitative T_1, T_2, T_2^*, $T_{1\rho}$, or spin density contrast (*11, 14, 17*). One of the advantages of the use of the technique is the almost direct implementation in existing imaging scanners, with minimal hardware modifications. Although single-point methods may suffer from long acquisition times, ramped magnetic field gradients (SPRITE) and considerations of repetition time effects on the resolution and signal-to-noise ratio (*17*) have resulted in a great time improvement. A recent book chapter describes the range of applicable systems and compares the SPRITE method to other short T_2^* imaging techniques (*20*).

Unlike projection reconstruction techniques, SPRITE is able to sample the *k*-space origin with high precision. *K* space is sampled in a rectilinear fashion and data regridding is not required prior to Fourier reconstruction. SPRITE gas phase imaging is not restricted to noble gases with long T_1 relaxation times and the technique does not have a linewidth restriction on resolution. The technique is able to exploit the short T_1 relaxation times which are common due to spin rotation relaxation in gases and benefit from enhanced relaxation due to surface interactions.

Diffusion effects in SPRITE can be estimated (*21, 22*) and consequently it is shown in the present report that, once the image field-of-view is chosen, optimum ways of setting the maximum amplitude of the phase encoding gradient and the encoding time can be computed. A separate section presents a discussion on this matter. The restricting factors for the total acquisition time are also discussed in this work.

Under Results, examples of one- and three-dimensional proton and fluorine gas imaging are presented. A discussion of magnetization preparation for T_1 and T_2 contrast (*14, 15*) and new considerations on SPRITE centric *k*-space sampling (*17*) are presented elsewhere.

SINGLE-POINT IMAGING CONSIDERATIONS

Sampling

Single-point imaging is a pure phase encoding MRI method. The signal is acquired at a time t_p after the RF excitation pulse (*12*). In the case of a short signal lifetime, the excitation and acquisition are performed in the presence of phase encoding gradients.

With a constant encoding time, the signal for a one-dimensional profile is proportional to

$$S(k,t)=\int_{-\infty}^{\infty}\exp\left[-\frac{t_p}{T_2^*(x)}\right]R(x,t)\rho_0(x)\exp(i2\pi kx)dx, \quad [1]$$

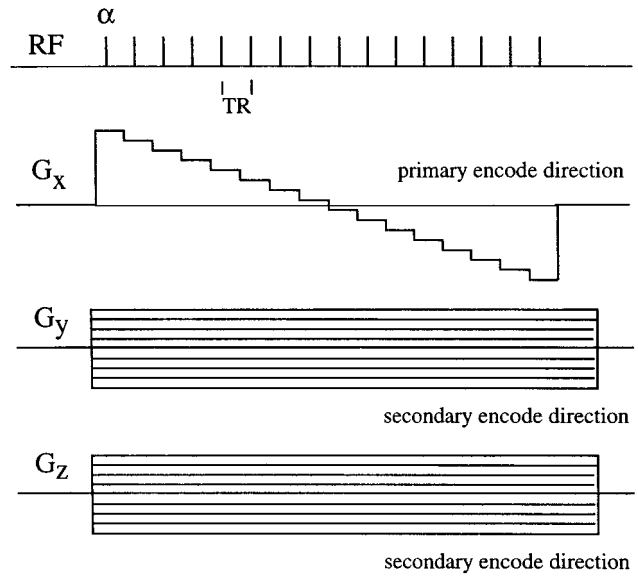

FIG. 1. Three-dimensional SPRITE pulse sequence. The RF pulses are applied with a repetition time TR, and the acquisition is performed at a time t_p after each excitation. The minimum encoding time t_p is determined by the instrument deadtime. A single point at constant t_p is acquired as a function of gradient amplitude, making this a pure phase encoding technique. A significant delay time between each successive ramp of the primary phase encoding gradient may be required for gradient cooling.

with $k=\gamma/2\pi\int_0^{t_p}G(t')\,dt'$ and γ the gyromagnetic ratio of the nuclei under study. $R(x,t)$ is a function that depends on the modulation of the signal during the acquisition. Note that for a small number of scanned points, n, the difference between summation and integration over all pixels in real space and j number in reciprocal space may be significant.

Only the case of constant gradient during the encoding time is considered here; then $\int_0^{t_p}G(t')\,dt'\equiv G\,t_p$. The acquisition process is repeated with n gradient steps between $-G_{max}$ and $+G_{max}$ [$k=(j-n/2)/\Delta x$, $0\le j<n$ (full *k*-space sampling)], where the field-of-view, $\Delta x=\pi n/\gamma t_p G_{max}$, is determined after Fourier transformation of the *k*-space signal. Notice that in spite of the constant encoding time, the magnetization evolution during the full *k*-space scanning is reflected in the explicit time dependence of the signal, $S(k,t)$. With no preparation pulses and if diffusion and saturation effects can be neglected, $R(x,t)=1$ and $S(k,t)=S(k)$.

The T_2^* term in Eq. [1] dominates when scanning at the center of *k* space. However, as the field gradients are incremented, the spin dephasing due to the gradient becomes faster than the spin–spin dephasing, resulting in the predominance of the last term of the integral factor.

Figure 1 shows a three-dimensional SPRITE pulse sequence. During the measurement the gradient is rapidly switched in a stepwise manner (*11*) and consequently longitudinal magnetization evolution may significantly modulate the signal during the gradient ramp. The resulting convolution may cause image blurring. The magnetization time evolution is considered by

introducing the time variable: $t = j$ TR, where TR is the repetition time for the RF excitation or equivalently the gradient step duration and j is the sampling number. This leads to

$$S(j) = \int_{-\infty}^{\infty} \exp\left[-\frac{t_p}{T_2^*(x)} \right] R(x, j)\rho_0(x) \times \Theta\left(\left| j - \frac{n}{2} \right| \right) \exp\left(ij2\pi \frac{x}{\Delta x} \right) dx, \quad [2]$$

where Θ is the pulse function defining the k-space sampling size:

$$\Theta\left(\left| j - \frac{n}{2} \right| \right) = \begin{cases} 1 & 0 \le j < n \\ 0 & j < 0 \text{ and } j \ge n \end{cases}. \quad [3]$$

Prior to a more detailed analysis presented in the following sections, a situation where the diffusion coefficient and the relaxation times are not space dependent is considered. The term corresponding to the T_2^* decay will produce signal attenuation without blurring. Then

$$S(j) \propto R(j)S_0(j) = R_{T_1}(j\text{TR})\, R_{\text{diff}}(j)S_0(j), \quad [4]$$

where $R_{T_1}(j\text{TR})$ represents the longitudinal magnetization evolution effect, $R_{\text{diff}}(j)$ is the diffusion modulation and $S_0(j)$ is the signal with only sampling modulation,

$$S_0(j) = \Theta\left(\left| j - \frac{n}{2} \right| \right) \int_{-\infty}^{\infty} \rho_0(x) \exp\left(ij2\pi \frac{x}{\Delta x} \right) dx. \quad [5]$$

Sources of signal intensity modulation on the k-space sampling produce a filter-like effect on the real space image. Because the image is determined by the convolution of the spin distribution and the Fourier transform of the modulation functions, the final resolution results from the largest width of all transformed functions. In particular, the sampling window resolution is the Fourier transform of $\Theta(|j - n|)$, which is proportional to $\text{sinc}((\pi n/\Delta x)x)$ and whose corresponding full width at half-height is

$$\text{FWHH}_k = 1.2 \frac{\Delta x}{n}, \quad [6]$$

where $\Delta x/n$ is the pixel size.

As shown below, the FWHH, corresponding to any of the mentioned factors, can determine the image resolution. In the next two sections, modulations due to molecular diffusion and longitudinal relaxation during k-space sampling are analyzed.

Diffusion Effects

The characteristic high molecular mobility in the gas phase frequently plays an important role in the image resolution and sensitivity.

Molecular diffusion in the presence of magnetic field gradients produces an irreversible attenuation which modulates the k-space signal, restricting the manipulation of the pulse sequence parameters. When the magnetic field inhomogeneity is linear, the attenuation results in (*22–24*)

$$R_{\text{diff}} = \exp\left(-\frac{D\gamma^2 G^2 t_p^3}{3} \right), \quad [7]$$

where D is the diffusion coefficient. This modulation is independent of the profile order and can be written as

$$R_{\text{diff}}(j) = \exp\left[-\left(j - \frac{n}{2} \right)^2 \frac{4D\gamma^2 G_{\max}^2}{3n^2} t_p^3 \right] = \exp\left[-\left(j - \frac{n}{2} \right)^2 \frac{4\pi^2 D}{3\Delta x^2} t_p \right], \quad [8]$$

showing that once the field-of-view and the number of points are chosen, the shortest encoding time produces the minimum diffusion effects.

Based on the linewidth (FWHH) of the $R_{\text{diff}}(j)$ Fourier transform, the resolution is reduced by the diffusion modulation when

$$\frac{\text{FWHH}_{\text{diff}}}{\text{FWHH}_k} \cong 1.6 \frac{n\sqrt{Dt_p}}{\Delta x} > 1, \quad [9]$$

or equivalently,

$$t_p > 0.39 \frac{\Delta x^2}{n^2 D}. \quad [10]$$

Using Einstein's equation and considering isotropic diffusion, the mean square molecular displacement during the observation time can be estimated by $\langle \delta x_{\text{diff}}^2(t_p) \rangle = 2\, D\, t_p$. The image is blurred by diffusion if

$$\left(\frac{\Delta x}{n} \right) < 1.3 \sqrt{\langle \delta x_{\text{diff}}^2(t_p) \rangle}. \quad [11]$$

This shows the expected result, namely that the resolution is coarser due to molecular diffusion when the mean square displacement during the phase encoding time is of the order of, or larger than, the sampling pixel size. Therefore the short encoding times in the SPRITE sequence are a major advantage and indeed it is possible to rationally choose an encoding time

t_p to minimize diffusion effects given an estimate of the diffusion coefficient and nominal pixel size. Note that since the *k*-space origin in SPRITE is acquired in the absence of magnetic field gradients, diffusion through imaging field gradients does not attenuate the image intensity, contrary to the case for gradient and spin echo imaging methods. Cory has discussed the sensitivity and resolution comparison of frequency encoding and pure phase encoding for liquid state microscopy (*21*, *22*).

T_1 Relaxation Effects

Intensive signal averaging is frequently required in SPI-based methods in order to overcome signal-to-noise limitations. This may result in a lengthy acquisition, unless a short repetition time is used. Thus, image resolution and sensitivity effects by longitudinal magnetization evolution during the scans must be thoroughly assessed.

In a SPRITE pulse sequence, the repetition rate is limited by the gradient amplifiers duty cycle rather than the gradient switching time, allowing for a significant reduction in the overall *k*-space scanning time. Strong gradient set mechanical vibrations produced during an SPI acquisition are eliminated by the small gradient field changes implemented in the SPRITE sequence.

Assuming a complete dephasing of transverse magnetization during the repetition period, the measured longitudinal magnetization for the order j pulse is (*25*)

$$M(j) = M_{ss} + (M_{init} - M_{ss})\exp\left(-j\,\frac{TR}{T_{1app}}\right), \qquad [12]$$

where the apparent relaxation time has been defined as

$$T_{1app} = \frac{T_1}{1 - \dfrac{T_1}{TR}\ln(\cos\alpha)}, \qquad [13]$$

and α is the flip angle determined by the RF pulse duration, t_α. The observed magnetization M_{init} in Eq. [12] is the magnetization for $j = 0$, and M_{ss} is the steady-state or asymptotic value

$$M_{ss} = M_0\,\frac{1 - \exp\left(-\dfrac{TR}{T_1}\right)}{\left[1 - \exp\left(-\dfrac{TR}{T_1}\right)\cos\alpha\right]}\sin\alpha, \qquad [14]$$

with M_0 the equilibrium magnetization. The pulse duration, t_α, is limited by the condition of uniform excitation of the entire sample so that

$$t_\alpha \cong \frac{1}{\text{bandwidth}} \leq \frac{4\pi}{\gamma G \Delta x}. \qquad [15]$$

Using Eqs. [12] and [14], the longitudinal relaxation modulation effect during the *k*-space scanning can be written as

$$R_{T_1}(j\text{TR}) = 1 + \epsilon\exp\left(-j\,\frac{TR}{T_{1app}}\right); \quad \epsilon = \frac{M_{init}}{M_{ss}} - 1. \qquad [16]$$

In the absence of magnetization preparation through dummy scans or other pulses (*17*), $M_{init} = M_0 \sin\alpha$, and

$$\epsilon = \frac{1 - \cos\alpha}{\exp\left(\dfrac{TR}{T_1}\right) - 1}. \qquad [17]$$

The sensitivity factor, i.e., signal-to-noise per unit of time, is proportional to M_{ss} while ϵ represents the relative signal intensity affected by magnetization evolution blurring. A small flip angle causes $\epsilon \approx 0$ and $R_{T_1}(j\ \text{TR}) \approx 1$, in which case no distortion is produced in the image.

For large flip angles and/or short repetition times the ϵ factor in $R_{T_1}(j\ \text{TR})$ becomes significant. In a sequential profile order, the T_1 modulation resolution is computed by the linewidth of its (Lorentzian) Fourier transform

$$\text{FWHH}_{T_1} = \frac{\Delta x\,\text{TR}}{\pi T_{1app}}. \qquad [18]$$

This simple relation shows that when the condition [19] is met, the image resolution is affected by the longitudinal magnetization evolution during the scan (*17*),

$$\frac{TR}{T_1} > \frac{\pi}{n} + \ln(\cos\alpha). \qquad [19]$$

On the other hand, as TR increases ϵ decreases and the signal affected by this resolution rather than the sampling pixel size becomes small. When repetition times are shortened, and unless the flip angle is reduced accordingly, the transient term dominates, $\epsilon \gg 0$ and $M_{ss} \ll M_0$, so the sensitivity loss would be severe and further discussion of the resolution factor may become irrelevant. For a 128-pixel image the relation of Eq. [19] is achieved for flip angles greater than 12°.

If the sensitivity is dictated by the steady state term,

$$s = s_0\,\frac{M_{ss}(\text{TR},\,\alpha)}{\sqrt{\text{TR}}}, \qquad [20]$$

where s_0 is a normalizing constant. The denominator stands for the variation in the number of scans as TR is changed keeping

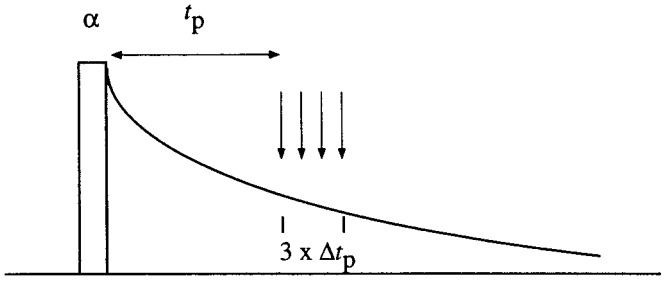

FIG. 2. SPRITE with multiple-point average. A four-data-point collection is shown, where each acquisition is separated by an interval Δt. The field gradients, omitted in the figure, were switched in the same fashion as presented in Fig. 1.

the overall acquisition time constant. In order to maximize the sensitivity, an increase in the number of averaging cycles can be accomplished by reducing TR while following the optimum angle condition. When no spoiling is applied, TR of the order and shorter than T_2 introduces oscillatory transients and then unwanted echoes.

While the molecular diffusion effect is driven by the choice of encoding time, the longitudinal magnetization evolution effect is driven by the excitation pulse rate. This makes the resolution and sensitivity considerations for the SPI method essentially different from those of spin-echo imaging techniques. Moreover, a clear advantage of the SPI-based technique is reached when the gradient switching time is of the order or longer than the transverse relaxation time of the sample.

Increased contrast in a heterogeneous sample may be achieved by manipulation of the initial magnetization (*26*) and by centric order acquisition (*17*).

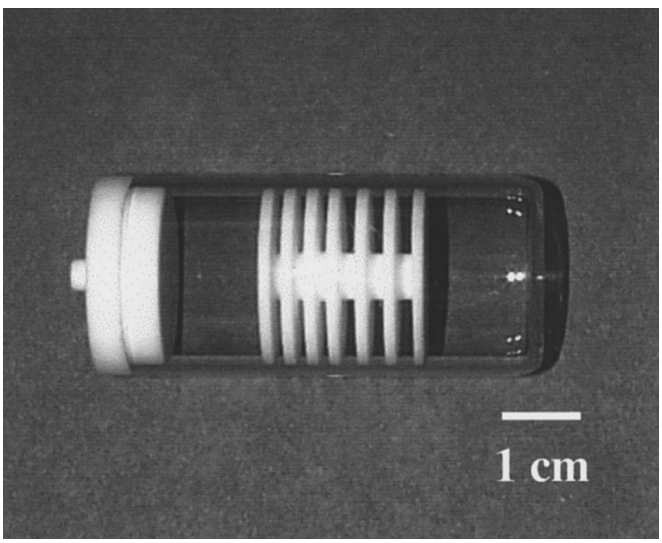

FIG. 3. Methane gas phantom. The 32-mm id glass container had a Teflon cap and spacers. The central piece has three 2-mm and three 3-mm grooves, separated by 2-mm walls. The overall gas volume could be varied by using different end caps.

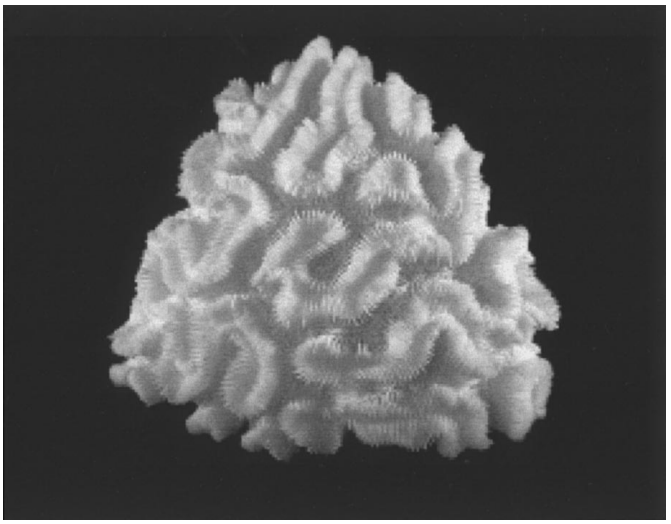

FIG. 4. Photograph of the brain coral *Diploria labyrinthiformis.* The highly porous coral sample has structure at a variety of length scales. The undulating fissures in the coral surface reveal high porosity, low density structures which penetrate the coral interior.

Multiple-Point Averaging

A significant sensitivity increase can be accomplished by an alternative acquisition modality, the imaging by multiple-point average, MPA. For each gradient step, a series of data points is collected instead of a unique value (*27*). The sampling resolution is dictated by the shortest phase encoding time, while the field-of-view is limited by the longest encoding time. The total sampling interval should be brief, as discussed below. Figure 2 displays the MPA sequence for a 4-point acquisition. After the four separated images are produced, the data points are interpolated to a common grid and a unique image is obtained by intensity averaging. This approach gives an approximately twofold sensitivity increase.

Phase cycling during each gradient step is not performed because only phases relative to the RF pulse can be attained.

All images obtained during this sequence present the same T_1 relaxation modulation effect. For molecular diffusion driven resolution, following the discussion presented above, the resolution corresponding to the individual images is

$$\left(\frac{\mathrm{FWHH_{diff}}}{\mathrm{FWHH}_k}\right)_i = (0.51\gamma\sqrt{D}\,G_{\max})t_{pi}^{3/2}; \qquad [21]$$

the i value labels the collected points. This indicates that in spite of the actual pixel size reduction, image blurring is present for fast molecular diffusion specimens. Thus, when points are scanned at longer times, the signal intensity loss and image blurring should be estimated.

The receiver bandwidth is not relevant for the basic SPI/SPRITE method but the filter width should be carefully evaluated for MPA experiments. In order to benefit from the MPA

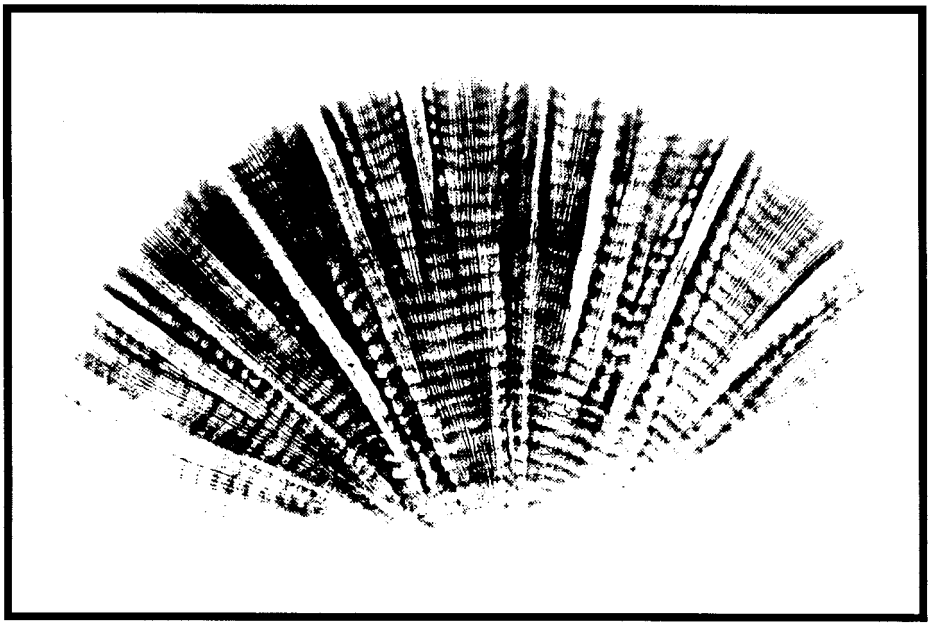

FIG. 5. X-ray-positive image of a 0.5-cm slice of coral *Diploria labyrinthiformis* (same colony as in Fig. 4). In this plane, the high porosity, low density surface features of Fig. 4 appear as radial channels from the coral interior to the surface (top of figure). The X-ray image has magnification ×1.

modality, the inverse of the data collection interval, $1/\Delta t_p$, should be less than the receiver filter width. Otherwise no significant difference would be noticed among the individual images (noise is not random between points), aside from the discussed resolution effect and the attenuation when the interval is significant compared to T_2^*. The receiver filter is set to cover the frequency range determined by the maximum gradient strength, $\nu_{rec} = \gamma G_{max} L/2\pi$, with L the distance from the center of the image to the most distant object point.

Setting the optimal receiver filter results in a reduction of the signal noise, but MPA produces a further SNR increase, even when the receiver filter is wider than the frequency spread of the object. The longest encoding time, $t_p = t_{p\,max}$, determines the smallest field-of-view, where $L \sim \Delta x/2$ and $\nu_{rec} = n/4t_{p\,max}$. Under optimum sensitivity conditions, $t_p = T_2^*/2$ (*21*), the time interval is selected based on

$$t_p \gg \Delta t_p > \frac{4t_{p\,max}}{n}. \qquad [22]$$

TABLE 1
Effect of Repetition Times on the Steady-State Magnetization, M_{ss}, and Image Sensitivity, s, for a Flip Angle of $\alpha = 50°$

TR/T_1	M_{ss}/M_0	$s(\mathrm{TR}/T_1)/s(\mathrm{TR}/T_1 = 2)$
0.5	0.49	1.3
1	0.63	1.2
2	0.73	1

Note. See Eq. [14]. As TR changes, the number of pulses varies to maintain a constant imaging time.

It should be noticed that only when the condition [22] is met an $\sqrt{m}$-fold increase in the sensitivity is achieved, where m is the number of scanned values per gradient amplitude. Covering a large time interval to extract local T_2^* information is not performed because of the field-of-view restriction determined by the change of encoding time under the same field gradient ramp.

EXPERIMENTAL

A homebuilt 32-rod birdcage resonator (*28*) in a 2.4-T 32-cm horizontal bore superconducting magnet (Nalorac Cryogenics Inc., Martinez, CA) was used. The probe was driven by a 2-kW RF amplifier (AMT, Brea, CA); its resonance range (90 to 100 MHz) allowed for tuning at both fluorine and proton frequencies. A water-cooled 7.5-cm id gradient set generated maximum gradients of 20 G/cm with a Techron 7780 amplifier. Experiments were controlled by a Tecmag (Houston, TX) Libra S-16 console. Pulse sequence generation and data collection were controlled by MacNMR software.

Two gases were imaged in this study: methane (CH_4, Air Liquide) and sulfur hexafluoride (SF_6, Canadian Liquid Air Ltd.). The latter is an inert, nontoxic gas (*4*). In order to avoid spurious signal, the resonance probe holder and shielding materials are constructed to provide proton- and fluorine-free conditions, as required.

Methane gas was imaged inside a glass bottle with a Teflon phantom (Fig. 3). The 32-mm od cylindrical phantom had three 2-mm and three 3-mm grooves, all separated by 2-mm walls. The fluorinated gas was imaged inside a $30 \times 30 \times 50$ mm^3 brain coral *Diploria labyrinthiformis* (Linnaeus) from Ber-

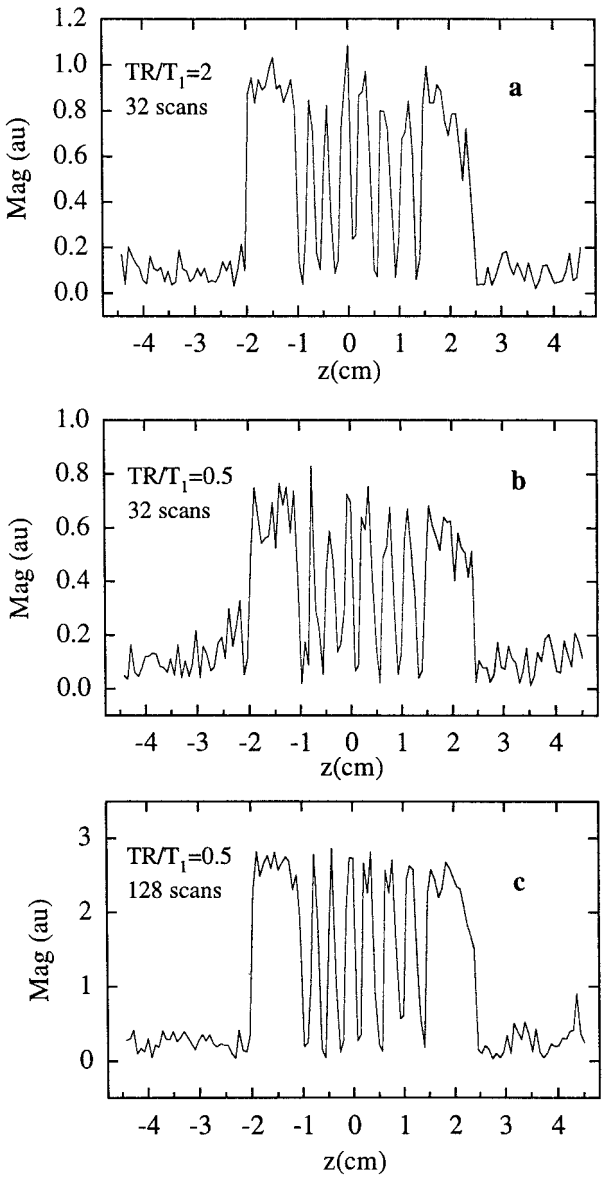

FIG. 6. SPRITE one-dimensional magnitude profiles of methane gas in the phantom of Fig. 3, G_{max} = 1.5 G/cm, t_p = 820 μs. Flip angle is kept constant, (a) 32 scans with TR = 2 T_1. (b) Same number of scans as in (a) with TR four times shorter, presenting lower signal-to-noise ratio and lower sensitivity. (c) Four times more scans than (a) but same overall acquisition time, resulting in a clear sensitivity increase.

muda (*29*). A photograph of the original coral used for this investigation is shown in Fig. 4 and an X-ray-positive image of a 5-mm slice is displayed in Fig. 5.

RESULTS AND DISCUSSION

Methane SPRITE

Methane was chosen as our prototype ^{1}H gas. Bulk relaxation times were measured: T_1 = 24 ± 1 ms, T_2 = 13.5 ± 0.7 ms, and T_2^* = 1.6 ± 0.1 ms in the phantom of Fig. 3. Effects of the longitudinal relaxation during the gradient ramp are predicted based on the discussion presented above. An RF pulse, 50° flip angle, is applied in the presence of the gradient, G_{max} = 1.5 G/cm, meeting the condition stated in Eq. [15]. In the highly sensitive proton-free birdcage resonator, protons from air are detected. This was confirmed by producing a profile of the probe signal without the sample and then pumping nitrogen gas into the gradient set. A clear signal reduction in the latter case is observed.

For this particular methane gas imaging example, profiles can be produced with comparable sensitivity by spin-echo techniques, but the optimum diffusion resolution is coarser than in the SPI case (*21*).

For a SPRITE 128-point profile, and following Eq. [19], image blurring is predicted even with short repetition times. On the other hand, for TR > T_2^* the small ϵ factor in Eq. [17] indicates that the final image resolution is dictated by the sampling size. Values of TR < T_1 result in low steady-state magnetization, but a maximum sensitivity is reached at TR/T_1 = 0.42.

Table 1 indicates that, in spite of the steady-state magnetization decrease with the repetition time, the image sensitivity increases as the number of scans is proportionally incremented

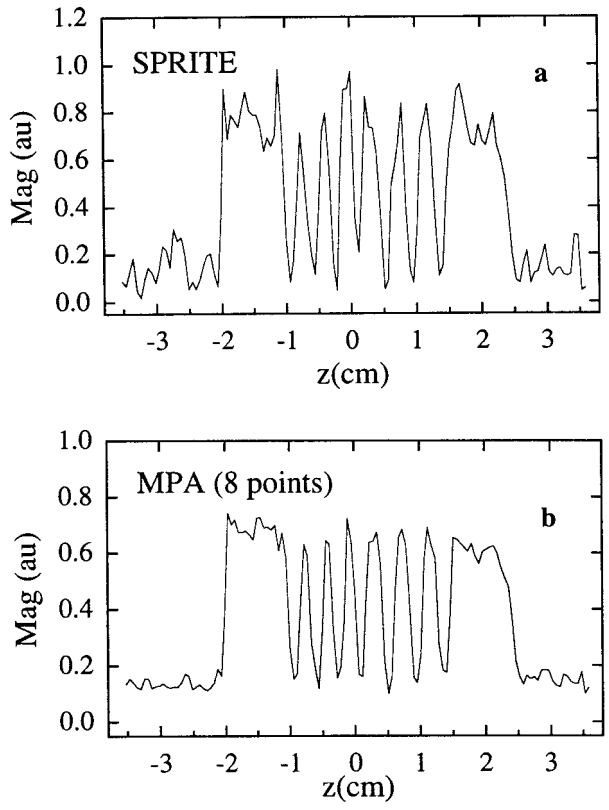

FIG. 7. Methane one-dimensional profiles obtained with 32 averages. The total acquisition time was 23 s. (a) 64-step SPRITE acquisition. (b) 8-point, 64-step multiple-point average acquisition with a 30-μs interval between acquisition points, showing a factor 2.3 sensitivity gain. G_{max} = 1.5 G/cm, t_p values are 820 to 1030 μs.

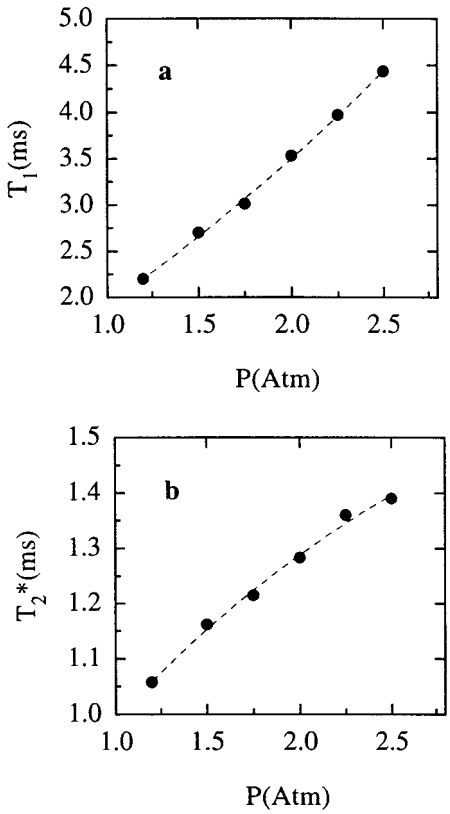

FIG. 8. Bulk ^{19}F measurements of sulfur hexafluoride (a) T_1 and (b) T_2^* relaxation times as a function of the gas pressure. Dashed curves are drawn as a guide to the eye.

in order to achieve the same total acquisition time. This suggests the use of shorter repetition times. The last column in Table 1 displays the sensitivity relative to large TR values. The reference $TR/T_1 = 2$ was arbitrarily chosen.

Figure 6 shows the profiles corresponding to two of the cases listed in Table 1. Optimum signal-to-noise and resolution are attained for $TR/T_1 \approx 0.5$ (Fig. 6c), with the same data collection time as for the profile shown in Fig. 6a. The profile in Fig. 6b presents lower signal-to-noise than the one with $TR/T_1 = 2$ and lower sensitivity than the one with 128 scans.

If a diffusion coefficient of 1 cm^2/s is assumed for the gas, following Eq. [9], $FWHH_{diff} \approx 0.6\ FWHH_k$, indicating that the image does not present additional blurring caused by the molecular diffusion modulation. In order to test this effect due to molecular diffusion a series of profiles was obtained with longer encoding times (see Eq. [10]), incrementing the gradient strength to keep the field-of-view unchanged. No effect was observed for a range up to 4 ms, where the signal loss by transverse relaxation becomes severe.

To show the benefits of the MPA technique, an 8-point acquisition was obtained. A $\Delta t_p = 30\ \mu$s delay between collected points was chosen to follow the condition indicated in Eq. [22]. Figure 7 shows the profiles for a 1-point SPRITE result and the average, after interpolation, of the MPA profiles. Notice the higher sensitivity accomplished. Given the difference in the encoding times, an 11% decrease of the signal intensity between the first and last image is observed due to T_2^* decay.

Sulfur Hexafluoride SPRITE

The natural abundance of ^{19}F (100%) and its high gyromagnetic ratio $\gamma_{19_F}/\gamma_{1_H} = 0.941$; absolute sensitivity = 0.83) make sulfur hexafluoride a good candidate for the present study. The first test was performed by pumping the gas into a Plexiglas container, while monitoring the pressure. Figure 8 shows the pressure dependence of the ^{19}F T_1 and T_2^* relaxation times. With this knowledge, the repetition times of the SPRITE experiment can be optimized. When the gas fills a heterogeneous sample or is mixed with another gas, the relaxation times should be reevaluated. According to Eqs. [14] and [18] and the results presented in Fig. 8, as the pressure of the gas is varied, resolution and sensitivity effects change significantly. For instance, for 90° flip angles and $TR/T_1 = 1$ at 1 atm the steady-state magnetization is doubled when the pressure is increased to 2.5 atm.

Gas phase SPRITE is likely to find a niche in studies of structure and dynamics of porous media. Therefore we have chosen a model porous limestone, a coral, as a realistic imaging phantom. Coral is advantageous, in part, because of the wide range of structure, at various length scales, which are readily apparent in Figs. 4 and 5. A coral sample was placed inside a rubber balloon. The balloon was inflated and emptied of the sample gas several times in order to attain high purity conditions. The final pressure was kept slightly above atmospheric values.

Although no dramatic changes in the relaxation parameters are expected given the large size of the coral voids, bulk

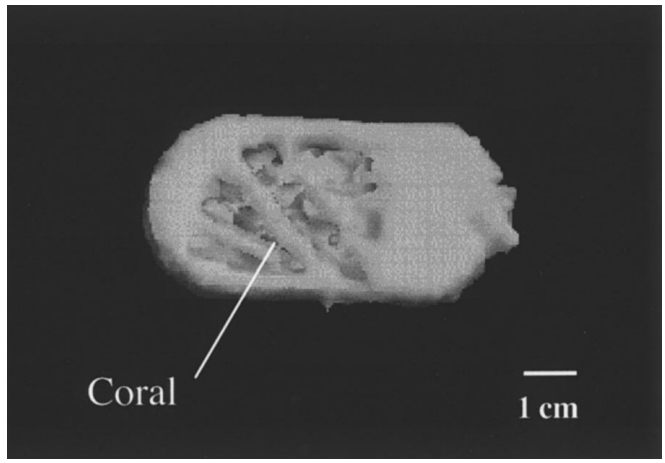

FIG. 9. Cut, surface rendered 3D ^{19}F image of sulfur hexafluoride distribution inside a gas-filled coral sample. The coral sample was placed inside a balloon enclosure. The rounded end of the balloon is visible at left, the tied neck at right. The encoding time $t_p = 320\ \mu$s, $G_{max} = 1.5$ G/cm, $\alpha = 50°$, and TR = 1.3 ms. The low-intensity radial channels (high porosity) of Fig. 5 appear in the MRI image as high signal radial channels with a similar geometry. Note the MRI sample is much smaller than the sample of Fig. 5.

relaxation times were measured in order to set the appropriate imaging parameters. An encoding time $t_p = 320\ \mu s$ was chosen to obtain optimum sensitivity with the observed T_2^* value of 600 μs. The maximum gradient strength of 1.5 G/cm allowed for excitation pulses of $t_\alpha = 25\ \mu s$ ($\alpha = 50°$) and a repetition time TR = 1.3 ms, without significant resolution loss for the measured $T_1 = 1.79(8)$ ms. Although $\mathrm{FWHH}_{T_1} \gg \mathrm{FWHH}_k$ (Eq. [18]), the contribution from this poor resolution to the final profile is small when compared to the sampling size resolution ($\Delta x/n = 2.5$ mm) contribution. As computed by Eq. [14], the steady-state magnetization is 60% of the equilibrium value. No diffusion-based blurring is predicted for a diffusion coefficient less than 80 cm^2/sec (Eq. [11])!

Under these conditions a three-dimensional $64 \times 64 \times 64$ image was obtained at a 6 min/scan rate. Figure 9 shows a rendered and cut 16-scan three-dimensional image with a field-of-view of $16 \times 16 \times 16$ cm. Note that the high porosity radial channels in the coral, which show minimal intensity in the X-ray-positive Fig. 5, are observed as high signal in the MRI image. This is presumably due to a high local gas density in these high porosity regions. Local T_2^* and/or T_1 differences may also effect the observed intensity. Studies with variation in the imaging parameters, t_p, TR, and α, would be required to fully assess the origin of the observed contrast (*14*, *17*).

CONCLUSIONS

The SPRITE technique has been used to produce images of ^{19}F and ^{1}H gases in phantom and porous media studies. New modalities in the pulse sequence allowed for a time-efficient acquisition. SPRITE overcomes the limitations of short relaxation times and large diffusion coefficients in the gas phase for common ^{1}H and ^{19}F containing gases. An *a priori* estimation of the optimum resolution and sensitivity attainable is achieved based on the evaluation of the modulation effects due to signal intensity evolution during the fast scan. A clear improvement over conventional echo methods can be obtained when the gradient switching times are of the order of, or longer than, the transverse relaxation time.

ACKNOWLEDGMENTS

We thank NSERC of Canada for operating (B.J.B., A.L.) and equipment (B.J.B., R.L.A.) grants and a NATO-NSERC fellowship (I.V.M.). We thank R. P. MacGregor for his assistance with the experiments and J. Cummings-Dickinson for her coral photograph (Fig. 4).

REFERENCES

1. R. L. Armstrong, Longitudinal nuclear spin relaxation time measurements in molecular gases, *in* "NMR 13 Basic Principles and Progress: Introductory Essays" (M. M. Pintar, Ed.), Springer-Verlag, Heidelberg (1976).
2. R. L. Armstrong, *Magn. Reson. Rev.* **12,** 91 (1987).
3. P. C. Lauterbur, *Nature* **242,** 190 (1973).
4. D. O. Kuethe, A. Caprihan, E. Fukushima, and R. A. Waggoner, *Magn. Reson. Med.* **39,** 85 (1998).
5. M. Albert, G. D. Cates, B. Driehuys, W. Happer, B. Saam, C. S. Springer Jr., and A. Wishnia, *Nature* **370,** 199 (1994).
6. H. Middleton, R. D. Black, B. Saam, G. D. Cates, G. P. Cofer, R. Guenther, W. Happer, L. W. Hedlund, G. A. Johnson, K. Juvan, and J. Swartz, *Magn. Reson. Med.* **33,** 271 (1995).
7. P. Bachert, L. R. Schad, M. Bock, M. V. Knopp, M. Ebert, T. Grobman, W. Heil, D. Hofmann, R. Surkau, and E. W. Otten, *Magn. Reson. Med.* **36,** 192 (1996).
8. M. E. Wagshul, T. M. Buttom, H. F. Li, Z. Liang, C. S. Springer, K. Zhong, and A. Wishnia, *Magn. Reson. Med.* **36,** 183 (1996).
9. J. P. Mugler III, B. Driehuys, J. R. Brookemann, G. D. Cates, S. S. Berr, R. G. Bryant, T. M. Daniel, E. E. de Lange, J. Hunter Downs III, C. J. Erickson, W. Happer, D. P. Hinton, N. F. Kassel, T. Maier, C. D. Phillips, B. T. Saam, K. L. Sauer, and M. E. Wagshul, *Magn. Reson. Med.* **37,** 809 (1997).
10. B. J. Balcom, P. J. Prado, R. L. Armstrong, and N. J. Shah, "Proceedings, Fifth ISMRM Conference, April 12–18, 1997," Vol. 1, p. 285, Vancouver, Canada.
11. B. J. Balcom, R. P. MacGregor, S. D. Beyea, D. P. Green, R. L. Armstrong, and T. W. Bremner, *J. Magn. Reson. A* **123,** 131 (1996).
12. S. Emid and J. H. N. Creyghton, *Physica* **128B,** 81 (1985).
13. D. E. Axelson, A. Kantzas, and T. Eads, *Canad. J. Appl. Spectrosc.* **40,** 16 (1995).
14. S. D. Beyea, B. J. Balcom, P. J. Prado, A. R. Cross, C. B. Kennedy, R. L. Armstrong, and T. W. Bremner, *J. Magn. Reson.* **135,** 156 (1998).
15. P. J. Prado, B. J. Balcom, S. D. Beyea, T. W. Bremner, R. L. Armstrong, R. Pishe, and P. E. Grattan-Bellew, *J. Phys. D* **31,** 2040 (1998).
16. C. B. Kennedy, B. J. Balcom, and I. V. Mastikhin, *Canad. J. Chem.* **76,** 1 (1998).
17. I. V. Mastikhin, B. J. Balcom, P. J. Prado, and C. B. Kennedy, *J. Magn. Reson.* **136,** 159 (1999).
18. B. J. Balcom, C. B. Kennedy, J. S. Dysart, A. Cross, and N. J. Shah, "Proceedings, ISMRM 6th Scientific Meeting, April 18–24, 1998," Sydney, Australia.
19. P. J. Prado, B. J. Balcom, and M. Jama, *J. Magn. Reson.* **137,** 59 (1999).
20. B. J. Balcom, SPRITE imaging of short relaxation time nuclei, *in* "Spatially Resolved Magnetic Resonance: Methods, Materials, Medicine, Biology, Rheology, Geology, Ecology, Hardware" (P. Bluemler, B. Bluemich, R. Botto, and E. Fukushima, Eds.), Wiley–VCH, Weinheim (1998).
21. S. Gravina and D. G. Cory, *J. Magn. Reson. B* **104,** 53 (1994).
22. S. Choi, X.-W. Tang, and D. G. Cory, *J. Imaging Syst. Technol.* **8,** 263 (1997).
23. D. E. Woessner, *J. Chem. Phys.* **34,** 2057 (1961).
24. K. R. Harris, R. Mills, P. J. Back, and D. S. Webster, *J. Magn. Reson.* **29,** 473 (1978).
25. M. T. Vlaardingerbroek and J. A. den Boer, "Magnetic Resonance Imaging," Springer, Berlin (1996).
26. B. Bluemich, *Concepts Magn. Reson.* **10,** 19 (1998).
27. P. J. Prado, B. J. Balcom, S. D. Beyea, R. L. Armstrong, and T. W. Bremner, *Solid State NMR* **10,** 1 (1997).
28. C. E. Hayes, W. A. Edelstein, J. F. Schenck, O. M. Mueller, and M. Eash, *J. Magn. Reson.* **63,** 622 (1985).
29. A. Logan and I. H. Anderson, *Bull. Marine Sci.* **49,** 847 (1991).